Conditions for Proton Temperature Anisotropy to Drive Instabilities in the Solar Wind

Simon Opie[1] , Daniel Verscharen[1] , Christopher H. K. Chen[2] , Christopher J. Owen[1] , and Philip A. Isenberg[3]
[1] Mullard Space Science Laboratory, University College London, Dorking, RH5 6NT, UK
[2] Department of Physics and Astronomy, Queen Mary University of London, London, E1 4NS, UK
[3] Space Science Center, University of New Hampshire, Durham, NH 03824, USA

Abstract

Using high-resolution data from Solar Orbiter, we investigate the plasma conditions necessary for the proton temperature-anisotropy-driven mirror-mode and oblique firehose instabilities to occur in the solar wind. We find that the unstable plasma exhibits dependencies on the angle between the direction of the magnetic field and the bulk solar wind velocity which cannot be explained by the double-adiabatic expansion of the solar wind alone. The angle dependencies suggest that perpendicular heating in Alfvénic wind may be responsible. We quantify the occurrence rate of the two instabilities as a function of the length of unstable intervals as they are convected over the spacecraft. This analysis indicates that mirror-mode and oblique firehose instabilities require a spatial interval of length greater than 2–3 unstable wavelengths in order to relax the plasma into a marginally stable state and thus closer to thermodynamic equilibrium in the solar wind. Our analysis suggests that the conditions for these instabilities to act effectively vary locally on scales much shorter than the correlation length of solar wind turbulence.

1. Introduction

The solar wind is a continuous stream of plasma from the Sun which exhibits significant measurable variability in its characteristic properties on a range of spatial and temporal scales (for recent reviews, see Matteini et al. 2012; Bruno & Carbone 2013; Chen 2016, and Verscharen et al. 2019). The fundamental processes that heat and accelerate the solar wind are not at present fully understood (Parker 1965; Tu & Marsch 1995; Cranmer et al. 2015).

A turbulent cascade is generally invoked to explain how energy injected near the Sun into the solar wind at large scales is transferred to kinetic scales, where it is available to heat and accelerate individual particles as the plasma travels radially outwards in a practically collisionless environment (Chandran et al. 2011; Alexandrova et al. 2013; Bruno & Carbone 2013; Kiyani et al. 2015). At kinetic scales, a secular energy transfer from electromagnetic field fluctuations into the particles ultimately increases entropy (Bale et al. 2009; Chen et al. 2016; Verscharen et al. 2016). In addition, energy transfer from the particles into the electromagnetic fields is possible when free energy in the form of temperature anisotropy or other nonequilibrium particle features is available. This transfer occurs in the form of instabilities that lead to characteristic wave–particle interactions. Microinstabilities act to restore thermodynamic equilibrium in the solar wind, thereby lowering the driving free energy (Kunz et al. 2014; Chen et al. 2016; Verscharen et al. 2017). In this way, microinstabilities play an important role for the macro-scale energy distribution in the solar wind (Verscharen et al. 2019).

The solar wind is often studied in a parameter space defined by the plasma β, given by the ratio of plasma pressure to the magnetic pressure, and the ratio between the temperature $T_\perp$ perpendicular to the magnetic field and the temperature $T_\parallel$ parallel to the magnetic field (Gary et al. 2001; Kasper et al. 2002; Hellinger et al. 2006; Bale et al. 2009). We refer to plots of the distribution of the data in this space for any given species in the solar wind as a $T_\perp/T_\parallel$–β plot. When contours of parameter combinations reflecting marginal stability to individual unstable modes are added to these $T_\perp/T_\parallel$–β plots, they demonstrate to what extent the temperature anisotropy is constrained by specific instability modes (Chen et al. 2016; Verscharen et al. 2016; Klein et al. 2018).

The best-fit constraints to proton temperature anisotropies in $T_\perp/T_\parallel$–β plots are typically provided by the thresholds for the oblique firehose and mirror-mode instabilities (Hellinger et al. 2006; Bale et al. 2009; Gary 2015), which are nonpropagating unstable modes of the Alfvén-mode and the slow-mode branches of the dispersion relation (Howes et al. 2006; Schekochihin et al. 2009; Kunz et al. 2015; Verscharen et al. 2017). Sufficient plasma pressure anisotropy creates the necessary conditions for the instabilities to act (Chandrasekhar et al. 1958; Parker 1958; Hasegawa 1969; Maruca et al. 2012; Kunz et al. 2014, 2015). At large scales, they are driven by anisotropies in the total pressure components of all species combined (Chen et al. 2016). In this work, we focus solely on the proton contribution to the total pressure anisotropy and the kinetic versions of these instabilities, which create fluctuations on a scale of the order of characteristic proton kinetic scales (Gary 2015; Howes 2015).

In the case of the oblique firehose instability, excess pressure parallel to the direction of the magnetic field causes the growth of bending in magnetic flux tubes. The magnetic tension force is unable to restore this bending if the pressure anisotropy is sufficiently large. Such a transverse perturbation does not propagate in the form of Alfvén waves (as it would in the absence of pressure anisotropy) but grows aperiodically with a polarization similar to Alfvén waves (Matteini et al. 2006;

Hellinger & Trávníček 2008; Kunz et al. 2014). For the mirror-mode instability, excess perpendicular pressure leads to the formation of quasi-periodic mirror structures trapping some of the ions between mirror points and setting up compressive standing waves with a wavevector oblique to the direction of the magnetic field (Kivelson & Southwood 1996; Kunz et al. 2016; Yoon et al. 2021). Particles accumulate in the region between the mirror points where the magnetic field strength is lower, acting to restore perpendicular pressure balance. This results in the mirror mode being characterized by anticorrelated fluctuations in density and magnetic field strength when seen by a traversing spacecraft (e.g., Russell et al. 1999). In both cases, the transfer of kinetic particle energy to the electromagnetic fluctuations coincides with a reduction in the anisotropy (Kunz et al. 2016; Yoon 2016).

Plasma instabilities are usually described in the context of homogeneous and steady-state plasma conditions (Gary 1993). However, the solar wind, like most natural plasmas, is turbulent and thus does not fulfill the assumptions applied in the standard theoretical treatment of these instabilities (Kivelson & Southwood 1996; Howes et al. 2008). Nevertheless, observations clearly show that instabilities act, at least at some time, in this environment (Matteini et al. 2012; Maruca et al. 2012; Wicks et al. 2016; Yoon et al. 2021). Our goal is to quantify the occurrence rates of oblique firehose and mirror-mode unstable solar wind intervals and their dependence on the direction of the magnetic field. We also measure the length of unstable intervals in order to evaluate statistically the spatial homogeneity requirement for these instabilities to effectively reduce the proton temperature anisotropy in the solar wind. If the occurrence of unstable intervals was determined by a scale-independent process, we would anticipate a smooth and scale-independent statistical distribution of the length scales of unstable solar wind intervals. However, if the effective action of the associated instabilities is scale dependent, we anticipate a break in the statistical distribution of the length scales of intervals with unstable plasma parameters. Even without knowing the underlying hypothetical distribution of length scales, we conjecture that a break in the statistical distribution into a steeper slope marks the length scale above which instabilities are effective. In this interpretation, the homogeneity assumption of linear theory is only sufficiently fulfilled in plasma intervals of lengths greater than the break scale in the statistical distribution.

2. Methods

2.1. Data Set

Recent space missions have been launched to study the inner heliosphere in great detail, with a focus on the processes that heat and accelerate the solar wind (Fox et al. 2016; Müller et al. 2020; Zouganelis et al. 2020). For this study, we use data from Solar Orbiter's Solar Wind Analyser (SWA; Owen et al. 2020) instrument suite, specifically the Proton Alpha Sensor (PAS) and the Magnetometer (MAG; Horbury et al. 2020). Solar Orbiter in situ data are publicly available at the Solar Orbiter Archive,[4] which is the source for all data in this study. We use data from the cruise phase of the mission in both 2020 and 2021.

SWA's PAS measures the 3D velocity distribution function (VDF) of protons and α-particles, whereby the VDF is

Table 1
Data Selection from the Solar Orbiter Archive with Approximate Heliocentric Distance for Each Data Set

Interval	Heliocentric Distance (R_S)	Number of Data Points
2020 Oct 7–18	205	185,923
2021 Apr 22–28	190	131,481
2021 May 5–11	180	131,849
2021 Jun 10–13	200	79,641
2021 Jul 6–11	190	117,427
2021 Jul 20–24	180	88,429
2021 Oct 9–12	150	81,362
2021 Oct 19–26	160	159,404

assembled over an interval of 1 s every 4 s, resulting in a normal-mode cadence of 0.25 Hz (Owen et al. 2020). The MAG fluxgate magnetometer provides eight magnetic field vectors per second in its normal mode (Horbury et al. 2020). We use the PAS proton ground moments data and the MAG normal-mode data in radial, tangential, and normal (RTN) coordinates. We average the corresponding MAG vector data over each 1 s VDF measurement interval from PAS.

For our statistical analysis, it is convenient to use continuous data intervals of reasonable length. In compiling the full data set, we select intervals of greater than three consecutive days, subject to data availability. We only include PAS data with a quality factor <0.2[5] and solar wind bulk velocity >325 km s^{-1} with initial selection by visual inspection of the data aided by the SWA-PAS data log.[6] The intervals chosen are listed in Table 1. The analyzed data set comprises 975,516 points in total. No attempt was made to eliminate structures such as shocks, interplanetary coronal mass ejections, or current sheets from the data set.

We rotate the proton pressure tensor to align with the magnetic field and create a time series for $\beta_\parallel \equiv 8\pi n_p k_B T_\parallel / B^2$, where n_p is the proton number density, k_B is the Boltzmann constant, and $\boldsymbol{B}$ is the magnetic field averaged over the associated 1 s PAS measurement interval. We then also calculate the ratio $T_\perp/T_\parallel$ for each PAS measurement.

2.2. Instability Thresholds

We base our analysis on the analytical approximation for the instability thresholds of the anisotropy-driven instabilities in the form

$$\frac{T_\perp}{T_\parallel} = 1 + \frac{a}{(\beta_\parallel - c)^b}, \qquad (1)$$

where a, b, and c are constants with values given for each instability by Verscharen et al. (2016). We use a maximum growth rate of $\gamma_m = 10^{-2}\Omega_p$, where Ω_p is the proton gyrofrequency. We evaluate these instability thresholds for the oblique firehose (OF) and for the mirror-mode (M) instabilities. For reference, we also include the instability thresholds for the Alfvén/ion-cyclotron (A/IC) and fast-magnetosonic/whistler (FM/W) instabilities in part of our analysis.
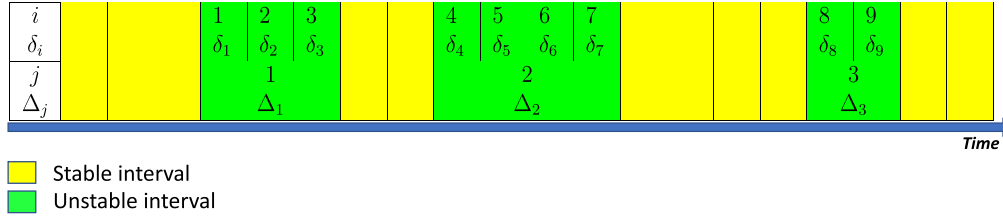
Figure 1. We identify unstable intervals and calculate their persistence interval (Δ_j) by aggregating the length scales (δ_i) of each measurement interval i in appropriate dimensionless units, where $\delta_i = V_i \tau / \rho_{pi}$, V_i is the bulk velocity in interval i, ρ_{pi} is the proton gyroradius in interval i, and τ is the interval duration (4 s). We also calculate δ_i in units of inertial length (d_{pi}) where ρ_{pi} is replaced by d_{pi}. We label sets of consecutive unstable intervals with the number j and calculate their length Δ_j with Equations (3) and (4).

2.3. Angle Analysis

Working in RTN coordinates, we calculate the angle between $\boldsymbol{B}$ and $\boldsymbol{V}$ using the complete 3D vectors as

$$\theta'_{BV} = \arccos \frac{\boldsymbol{B} \cdot \boldsymbol{V}}{BV}, \tag{2}$$

where $\boldsymbol{V}$ is the bulk velocity of the protons. We convert the angle θ'_{BV} into a full 360° distribution in order to capture the full range of variability in the fluctuations of the magnetic field and to retain the separation of the sector structure of the solar wind. For this conversion, we define $b = B_R + iB_T$ and $v = V_R + iV_T$. We then calculate the angle $\phi_v = \arg(v)$, where $\arg(\cdot) \in [0, 2\pi)$ is the polar angle in the complex plane. After rotating b by $-\phi_v$ in the complex plane, we define the difference angle between b and v as $\phi_{bv} = 180° \arg(be^{-i\phi_v})/\pi$. If $0 < \phi_{bv} \leqslant 180°$, we set $\theta_{BV} = 360° - \theta'_{BV}$. Otherwise, we set $\theta_{BV} = \theta'_{BV}$. This procedure leads to a representation of the angle θ_{BV} between $\boldsymbol{B}$ and $\boldsymbol{V}$ within the range [0°, 360°).

The angle θ_{BV} is the most appropriate measure for quantifying the fluctuations of $\boldsymbol{B}$ and $\boldsymbol{V}$ within structures convected over the spacecraft as a single point of measurement (see also Woodham et al. 2021, and references therein). This link to the convection speed $\boldsymbol{V}$ is particularly important when Taylor's hypothesis is used to map temporal to spatial data (Taylor 1938; Treumann et al. 2019). On average and for large data sets, we expect that $\theta_{BV} \approx \theta_{BR}$, where θ_{BR} is the angle between $\boldsymbol{B}$ and the unit vector $\hat{\boldsymbol{R}}$ in the radial direction. In the case of $\boldsymbol{V} \propto \hat{\boldsymbol{R}}$, θ_{BV} represents the azimuthal angle of $\boldsymbol{B}$ and statistically approaches the Parker angle (Parker 1965).

2.4. Length-scale Analysis

We calculate the length scales associated with the persistence of instabilities in the solar wind using Taylor's hypothesis (Taylor 1938). As indicated in Figure 1, we identify all intervals with parameters above an instability threshold from Equation (1) in the complete data set separately for oblique firehose and mirror-mode instabilities. Unstable intervals are shown as individual green boxes in Figure 1. We calculate the length scale $l_i = V_i \tau$ for each unstable interval i, where V_i is the proton bulk velocity of interval i and $\tau = 4$ s is the cadence of PAS. Using the proton gyroradius ρ_{pi} and the inertial length d_{pi} for each individual interval i, we then calculate the dimensionless length scales $\delta_i^\rho = l_i / \rho_{pi}$ and $\delta_i^d = l_i / d_{pi}$. The sums of the consecutive dimensionless length scales give the total dimensionless persistence interval for each occurrence of the respective instability as convected over the spacecraft. We

define them as

$$\Delta_j^\rho = \sum_i \delta_i^\rho \tag{3}$$

and

$$\Delta_j^d = \sum_i \delta_i^d, \tag{4}$$

where the index j indicates each set of consecutive unstable intervals, and the index i sums over all individual intervals that contribute to the persistence interval j.

3. Results

3.1. Data Overview

In Figure 2, we show the $T_\perp/T_\parallel$–$\beta_\parallel$ plot of the probability density function (PDF) of our full data set. From the total data set, 940,598 individual data points are stable to both the mirror-mode and oblique firehose instabilities, within the regime that we classify as both mirror stable and firehose stable; 4526 individual data points are in the mirror-mode unstable region (0.46%) and 30,392 individual data points in the oblique firehose unstable region (3.12%). The instability thresholds apparently bound the probability distribution, as has been noted by others (Hellinger et al. 2006; Bale et al. 2009).

The number of data points in the mirror-mode and oblique firehose unstable regimes is sufficient to allow a separate statistical analysis of these regions. For this investigation, we define four categories of data: "all" data represents the complete data set; "stable" refers to the data points that are stable to both the mirror-mode and the oblique firehose instabilities; and "oblique firehose unstable" and "mirror-mode unstable" refers to the data points in the regions beyond their respective instability thresholds with $\gamma_m > 10^{-2}\Omega_p$.

3.2. Angle Analysis

Figure 3 shows, by category of data points (all, stable, oblique firehose unstable, mirror-mode unstable), the distributions of θ_{BV}, calculated as described in Section 2.3. We quantify the rate of occurrence of unstable data for the oblique firehose and the mirror-mode instability by normalizing the distributions by the total number of occurrences of the whole data set in each angle bin. This normalization quantifies the statistical significance of the excess of unstable modes in each angle bin. We calculate the normalized distribution bin count:

$$\sigma_{ND} = \frac{\sigma_R}{\sigma_{TD}}, \tag{5}$$

where σ_R is the bin count of unstable intervals and σ_{TD} is the total bin count of the whole data set for a given angle. The
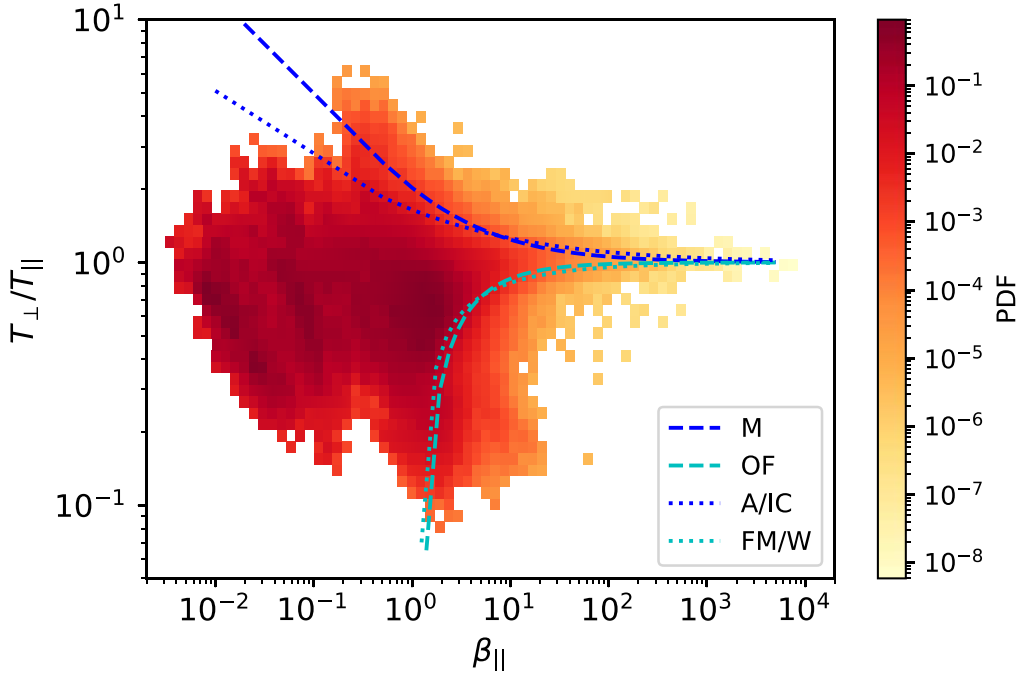
Figure 2. Data distribution in the $T_\perp/T_\parallel$–$\beta_\parallel$ plane. We overplot the instability thresholds according to Equation (1) for $\gamma_m = 10^{-2}\Omega_p$. The color-coding indicates the PDF of data points in each bin.

resulting polar plots represent the conformal projection of the 3D angle distribution onto a 2D (RT) plane.

Panels (b) and (c) of Figure 3 show a clear differentiation in the distribution of the data points that are oblique firehose and mirror-mode unstable. We find that oblique firehose unstable data points occur predominantly when $225° \lesssim \theta_{BV} \lesssim 270°$. The mirror-mode unstable data points occur predominantly when $\boldsymbol{B}$ and $\boldsymbol{V}$ are within $\sim45°$ of alignment or anti-alignment.

We note the uneven distribution of the direction of $\boldsymbol{B}$ between the sunward and anti-sunward sectors in our data set. Data in the upper-left quadrants of the plots, where $180° \leqslant \theta_{BV} \leqslant 270°$, predominate. We attribute this asymmetry to the position of the spacecraft relative to the current sheet under the quiet solar wind conditions during our data-collection period.

Figure 4 shows, by category of data points (all, stable, oblique firehose unstable, mirror-mode unstable), the probability densities of θ_{BV}, calculated as described in Section 2.3. For purposes of comparison, we plot the normalized density bin count

$$\sigma_N = \frac{\sigma_R}{\sigma_T W_b} \tag{6}$$

for each category, where σ_R is the bin count, σ_T is the total bin count of the plotted data set across all angle bins, and W_b is the bin width. This distribution is normalized so that $\sum(\sigma_N W_b) = 1$. The maxima of the PDF, shown by the peak values for the distribution of all data, are at $\theta_{BV} \approx 70°$ in the anti-sunward and $\approx225°$ in the sunward direction. The PDF of mirror-mode unstable points peaks and exceeds the PDF of stable points at $\theta_{BV} \approx 25°$, $155°$, $225°$, and $330°$, whereas the PDF of oblique firehose unstable points peaks and exceeds the PDF of stable points at $\theta_{BV} \approx 75°$ and $255°$.

We plot the distributions of $T_\perp$ and $T_\parallel$ against θ_{BV} for data points in the mirror-mode and oblique firehose unstable

categories in Figure 5. In both cases, the distributions of $T_\perp$ and $T_\parallel$ separately exhibit variability with θ_{BV} consistent with the pattern of angular dependence in Figure 4. Similar distributions for $\beta_\parallel$ (not shown here) do not reveal a marked dependence on θ_{BV}.

We explore the correlation between temperature anisotropy and θ_{BV} by investigating the mean values of $T_\perp$ and $T_\parallel$ as functions of θ_{BV} for the complete data set and for each of the unstable categories. For this calculation, we first sort all N_D data points in each of the data intervals by θ_{BV}, where N_D is the total number of data points in the interval. We then calculate a running mean over θ_{BV} for the separate parameters $T_\perp$ and $T_\parallel$ using a moving averaging window of length $0.04N_D$. The results are plotted as Figure 6.

We show the running mean for each of $T_\perp$ and $T_\parallel$ for the mirror-mode instability, the oblique firehose instability, and for all data in panels (a) through (c). For comparison, we show a similar running mean of T_R and T_{TN} in panel (d), where T_R is taken directly as the radial temperature from the RTN data set in the proton ground moments. T_{TN} is given by $(T_T + T_N)/2$, where T_T is the tangential temperature and T_N is the normal temperature.

3.3. Length-scale Analysis

In Figure 7, we show the PDFs of instability persistence for both oblique firehose and mirror-mode instabilities measured in units of the proton gyroradius and in units of the inertial length. Panels (a) and (b) show a power-law relationship with a distinct break (Δ_b^ρ) at $\sim34~\rho_p$ for the oblique firehose instability and at $\sim24~\rho_p$ for the mirror-mode instability. At scales smaller than the break, the dependence of the instability persistence PDF on Δ^ρ exhibits a shallow gradient. At larger scales, the fitted power-law relationship is appreciably steeper and shows an exponent of ≈-2.17 for both the oblique firehose instability and the mirror-mode instability. This exponent is consistent
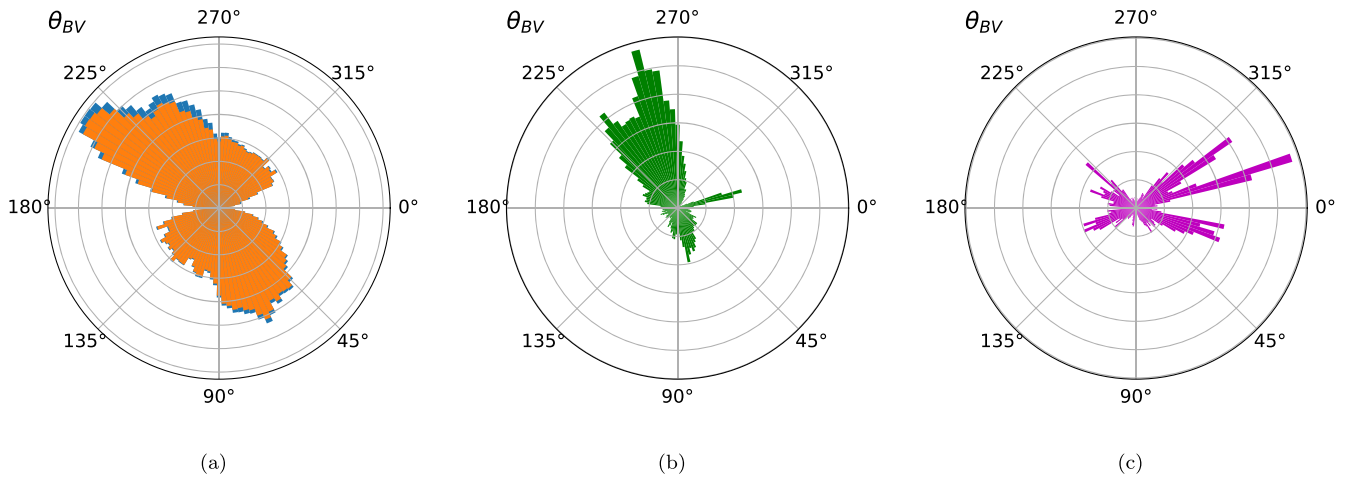
Figure 3. Polar plots of the distributions of the four categories of data points as functions of θ_{BV}. The three panels show (a) all data (blue) with stable data (orange) overlaid, (b) oblique firehose unstable data (green), and (c) mirror-mode unstable data (magenta). Both (b) and (c) are normalized according to Equation (5). The gray concentric circles are spaced in increments of (a) 2500, (b) 0.02, and (c) 0.005, starting from zero. 0° is the direction of V. The distributions are binned at 3° resolution.
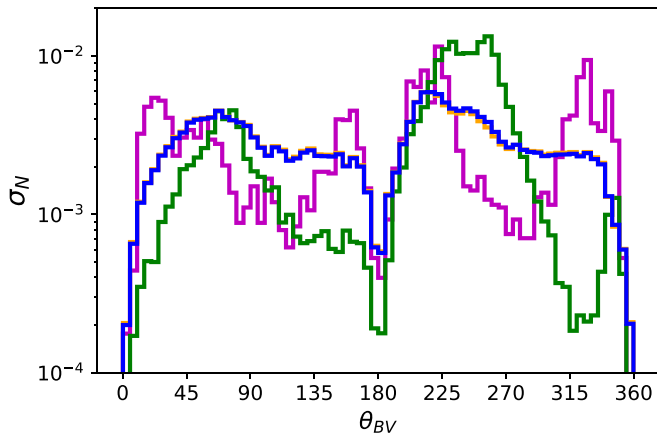
Figure 4. PDF of the angular distribution of our four data categories: all data (blue), stable (orange), oblique firehose unstable (green), mirror-mode unstable (magenta). The orange histogram is mostly obscured by the blue. The PDFs, calculated according to Equation (6), are binned at 5° resolution.

with those found for Δ^d in panels (c) and (d), although here break points are not readily identifiable.

According to previous studies (Gary 1993; Pokhotelov 2004), the maximum growth rate of the oblique firehose and mirror-mode instabilities occurs when $k_w \rho_p \approx 0.5$, where k_w is the wavenumber. The associated instability wavelength at maximum growth is then given by

$$\lambda_w = \frac{2\pi}{k_w} \approx \frac{2\pi \rho_p}{0.5}. \quad (7)$$

Comparing with Δ_b^ρ above, Equation (7) indicates that the space required for the instabilities to act is $\sim 2.7\ \lambda_w$ for the oblique firehose instability and $\sim 1.9\ \lambda_w$ for the mirror-mode instability.

4. Discussion

4.1. Dependence on Measurement Cadence

By contrast with most previous studies, we find a more extensive distribution of data points in the unstable regions of our $T_\perp/T_\parallel - \beta_\parallel$ plot in Figure 2. This difference is likely due to the higher sampling cadence of PAS at 4 s in normal mode

(Owen et al. 2020) than, for example, that of the WIND Solar Wind Experiment (SWE) instrument. SWE has a cadence for its Faraday cup ion sensor of 92 s (Ogilvie et al. 1995; Maruca & Kasper 2013) and is the data source for many earlier studies (Hellinger et al. 2006; Bale et al. 2009; Maruca et al. 2012; Chen et al. 2016; Verscharen et al. 2016). PAS's higher cadence enables the instrument to sample characteristic features of the solar wind without averaging over variations in the distribution at timescales greater than a few seconds (Verscharen & Marsch 2011; Nicolaou et al. 2019).

We demonstrate the impact of longer sampling times by averaging our data set in Appendix A. In Figure 8, we show the consequent decrease in the proportions of data points in the mirror-mode and oblique firehose unstable regions with increasing measurement cadence. Although we observe in our data widespread distributions of data points in the parts of parameter space characterized as unstable according to Equation (1), the overall pattern of regulation by nonpropagating instabilities ultimately remains consistent with the earlier work.

4.2. Interpretation of Our Angle Analysis

For our analysis, we divide the polar plot in Figure 3 into eight segments of 45° arcs. We define the four segments between 315° and 45° and between 135° and 225° as "quasi-parallel" with respect to the flow direction of the solar wind. We define the other four segments as "quasi-perpendicular" with respect to the flow direction of the solar wind.

The oblique firehose instability is driven by $T_\parallel > T_\perp$ which, according to Figure 3(b), most frequently corresponds to excess pressure in the direction quasi-perpendicular to the flow velocity. This direction is also approaching alignment with the Parker spiral angle. The mirror-mode instability is driven by $T_\perp > T_\parallel$ which, according to Figure 3(c), most frequently also corresponds to excess pressure in the direction quasi-perpendicular to the flow velocity. This finding suggests that the expansion direction plays a crucial role for the generation of plasma conditions that drive both oblique firehose and mirror-mode instabilities. However, the large-scale double-adiabatic expansion alone, according to the Chew–Goldberger–Low (CGL) prediction (Chew et al. 1956; Parker 1958; Matteini et al. 2007, 2012), does not produce this observed correlation.
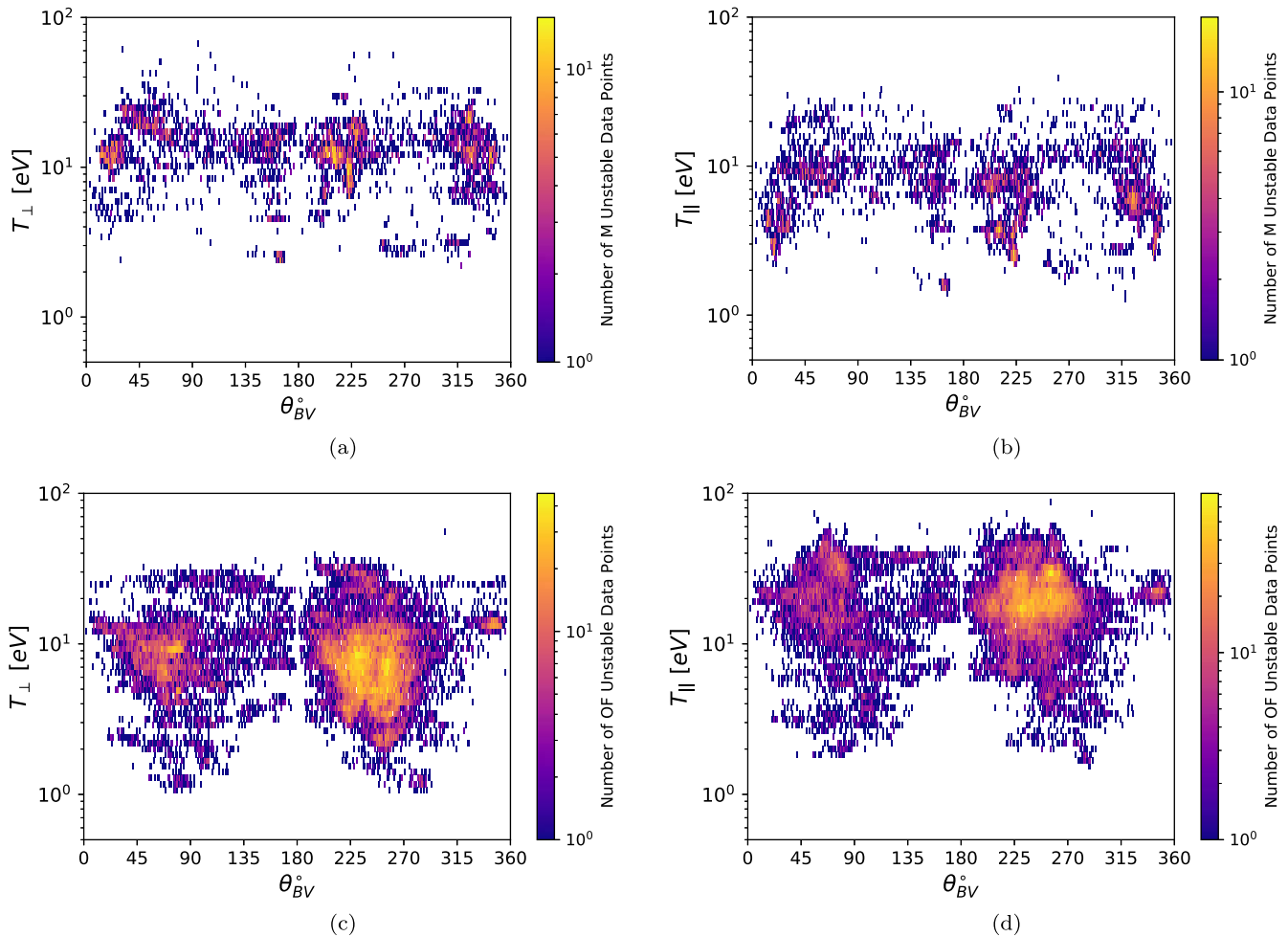
Figure 5. Dependence of $T_\perp$ and $T_\parallel$ on θ_{BV} in the solar wind. The upper panels ((a) $T_\perp$ and (b) $T_\parallel$) only include mirror-mode unstable points. The lower panels ((c) $T_\perp$ and (d) $T_\parallel$) only include oblique firehose unstable points. The color scale indicates the number of data points per bin.

In fact, the observed correlations are opposite to the expectations from CGL expansion alone, as shown in Appendix B. Instead, we must invoke a non-CGL expansion of the ions, which is a known observational result (Marsch et al. 2004; Matteini et al. 2007) and confirmed by the analysis of the two-fluid thermal energy equation (e.g., Hellinger et al. 2013).

A possible explanation for the angular dependency of the PDF for the oblique firehose and mirror-mode instabilities lies in the presence and variability of local, large-scale Alfvénic fluctuations. These fluctuations lead to a time variation in θ_{BV} at the location of the spacecraft (D'Amicis et al. 2019). Greater amplitudes of large-scale Alfvénic fluctuations typically coincide with increased perpendicular ion heating in the solar wind (Bruno et al. 2004, 2006). This increased perpendicular heating often generates temperature anisotropy with $T_\perp > T_\parallel$ and thus favorable conditions for the excitation of mirror-mode instabilities (Matteini et al. 2006; Yoon et al. 2021). As a consequence, we expect a statistically increased occurrence of mirror-mode unstable data points at times with large-amplitude Alfvénic fluctuations. These are more likely to be associated with θ_{BV} angles away from the direction of the Parker spiral than times without large-amplitude Alfvénic fluctuations (Bruno et al. 2004).

In this interpretation, we associate oblique firehose unstable intervals with solar wind parcels with low amplitudes of Alfvénic fluctuations. We expect a stronger average alignment of the distribution of these oblique firehose unstable intervals with the average θ_{BV} of the solar wind. This is consistent with Figures 3(a) and (b), which show that the distribution of oblique firehose unstable intervals is mostly aligned with the average direction of $\boldsymbol{B}$, representing the Parker spiral angle (Parker 1965)—notwithstanding the asymmetry of sampled sector structures in our data set.

Figures 6(a) through (c) demonstrate that the measured solar wind on average exhibits $T_\parallel > T_\perp$, so that conditions favorable for the excitation of the mirror-mode instability are the exception. However, panel (c) shows that, for all data, $T_\parallel$ and $T_\perp$ converge when $\boldsymbol{B}$ and $\boldsymbol{V}$ approach alignment or anti-alignment, which is consistent with the statistical distribution of the unstable data points in Figure 4. However, the sector asymmetry of our data set makes this convergence stronger in the case of $\theta_{BV} \sim 360°$.

The distributions of the unstable data as a function of θ_{BV} shown in Figures 3(b) and (c), together with the required temperature anisotropy to drive each of the instabilities, suggest that the mirror-mode and oblique firehose instabilities act predominantly when $T_{TN} > T_R$, where for the mirror-mode $T_{TN} \sim T_\perp$ and for the oblique firehose $T_{TN} \sim T_\parallel$. The mean values of the data set show that, on average, $T_R/T_{TN} = 0.985$ (all data), 0.447 (oblique firehose unstable data points), and 0.572 (mirror-mode unstable data points). Figure 6(d) shows
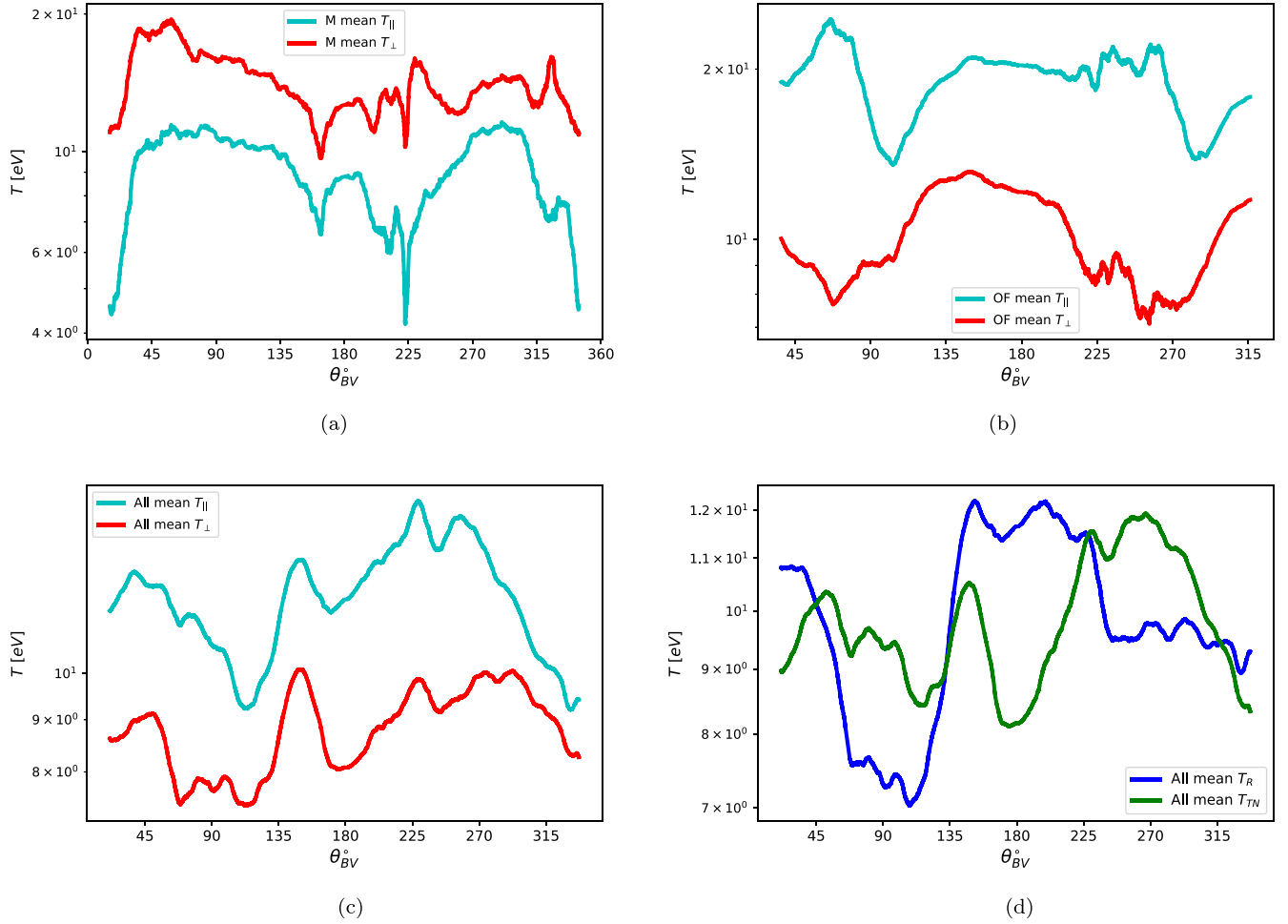
Figure 6. Panels (a)–(c) show the $T_\perp$ (red) and $T_\parallel$ (cyan) dependence on θ_{BV} in the solar wind for (a) mirror-mode unstable (b) oblique firehose unstable and (c) all data. Panel (d) shows the equivalent dependency of T_R (blue) and T_{TN} (green) for all data. The results shown are running means over θ_{BV} after sorting the data points by θ_{BV}.

the θ_{BV} dependence of T_R and T_{TN}, which derives from the general condition that $T_\parallel > T_\perp$ on average, as shown in Figure 6(c). The angular dependency of the observed oblique firehose unstable data is consistent with this variability, whereas the distribution of mirror-mode unstable data peaks at the values of θ_{BV} where the plots of T_R and T_{TN} intersect. We observe that these points of intersection are the limits to the values of θ_{BV} where both $T_{TN} \sim T_\perp$ and $T_{TN} \gtrsim T_R$.

4.3. Interpretation of Our Length-scale Analysis

In Figure 7, we find that our PDF of Δ^ρ steepens appreciably at the break point Δ_b^ρ. The break point is more clearly defined by length scales normalized in units of ρ_p than in units of d_p, which is expected since these instabilities grow on scales associated with the gyroscale rather than the inertial length (Howes et al. 2011; Matthaeus et al. 2014). We interpret the shallower PDF at $\Delta^\rho < \Delta_b^\rho$ as an indication that, in spatial intervals shorter than Δ_b^ρ, the instabilities are less efficient in reducing the temperature anisotropy to stable values than in intervals longer than Δ_b^ρ. The existence of this break point and the transition into a steeper slope at $\Delta^\rho > \Delta_b^\rho$ is consistent with our conjecture that the efficiency of oblique firehose and mirror-mode instabilities is scale dependent. In this interpretation, Δ_b^ρ represents the minimum length of plasma intervals with unstable parameters for which the instabilities efficiently

modify the plasma into a stable state. We interpret the difference in Δ_b^ρ between oblique firehose and mirror-mode instabilities as an indication that these instabilities set different requirements on the homogeneity of the unstable plasma volumes. We observe that the power-law index beyond the break point is consistent for both categories of unstable data and independent of our length-scale normalization. This universality suggests that the power laws themselves are representative of the underlying distribution of conditions that drive the analyzed instabilities in the solar wind.

We find that Δ_b^ρ corresponds to approximately 2–3 wavelengths of the unstable mode at typical maximum growth rates. This result suggests that the conditions needed for instabilities to act efficiently are bounded by spatial scales $\mathcal{O}(10^3 \text{ km})$ that are very short relative to the correlation length of solar wind turbulence, which has been measured as $\mathcal{O}(10^6 \text{ km})$ (Matthaeus & Goldstein 1982; Matthaeus et al. 2005). However, the evaluation of the influence of the turbulent cascade on linear processes requires a scale-dependent comparison of nonlinear and linear timescales (Matthaeus et al. 2014). While outside the scope of this study, it would be worthwhile to compare the scale-dependent eddy turnover times of the plasma turbulence at the scales of the unstable intervals. Such a comparison would allow the assessment of the timescales that potentially create and destroy the conditions
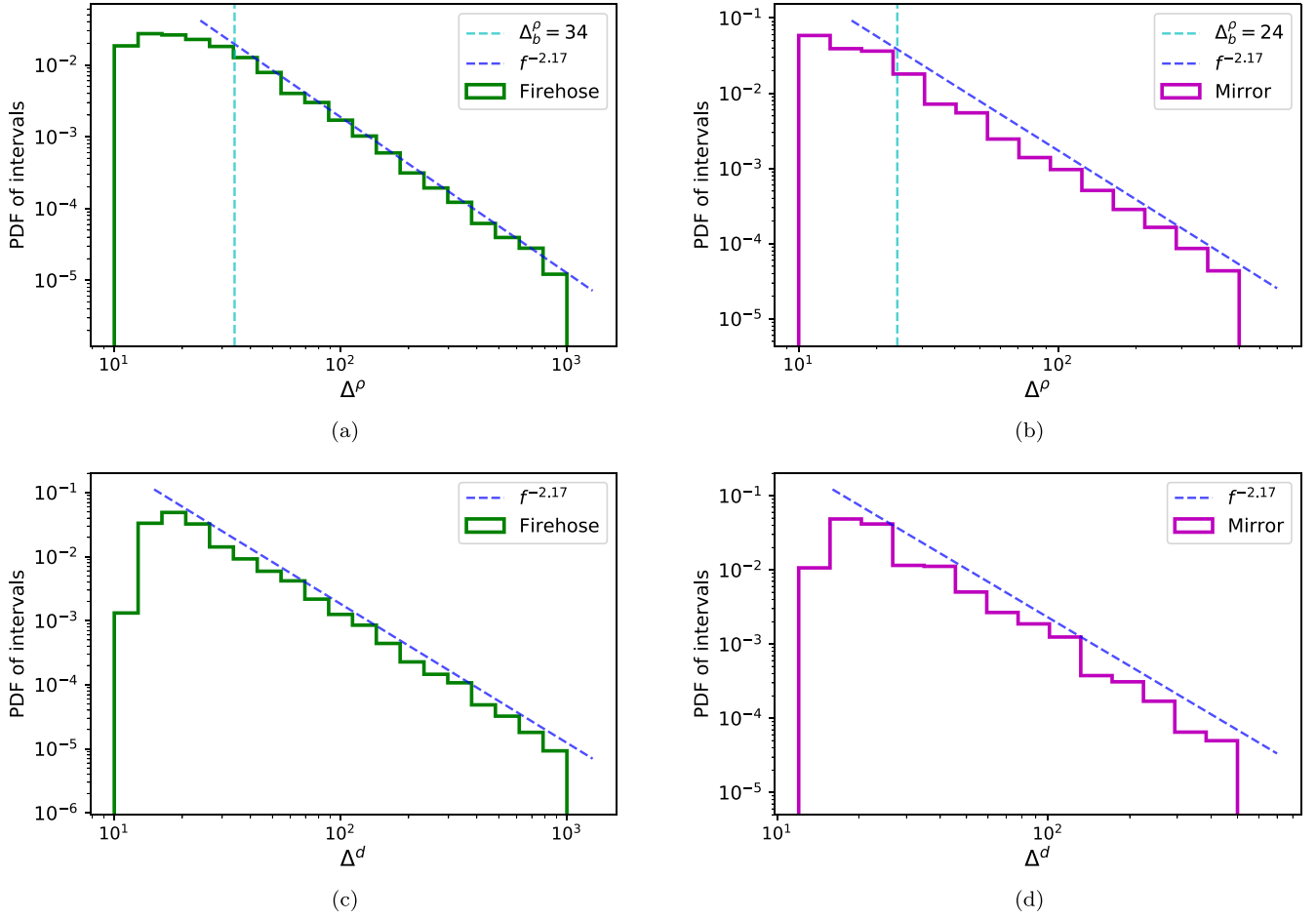
Figure 7. PDF plots of persistence intervals in length scale for oblique firehose (green) and mirror-mode (magenta) instabilities in the solar wind. Panels (a) and (b) show the length scale in proton gyroradii (Δ^ρ). Panels (c) and (d) show the length scale in proton inertial lengths (Δ^d). We indicate break points at Δ_b^ρ with cyan vertical lines and power-law fits in dark blue, giving power indexes of $\approx$–2.17 for both the oblique firehose and the mirror-mode instability.

required for instabilities to act (Klein et al. 2017, 2018; Qudsi et al. 2020).

In our study, we assume Taylor's hypothesis to link temporal variations in the measurements with spatial variations in the solar wind. A single-spacecraft measurement is unable to disentangle temporal and spatial variations in the solar wind. Simulations show a temporal latency in the onset of the oblique firehose instability (López et al. 2022), which complicates the interpretation of the spatial persistence discussed in this work. The average temporal persistence of data points in the unstable regions of our $T_\perp/T_\parallel$–$\beta_\parallel$ plot is 10.33 s for the mirror-mode and 11.49 s for the oblique firehose instability. From these numbers, we infer that a sampling cadence of less than $\sim$10 s is needed to observe the full length-scale distribution of unstable regions in the solar wind in our data set. This cadence is equivalent to a spatial scale of $\sim$80ρ_p convected over the spacecraft, given the average values for V and ρ_p derived from our data.

4.4. Limitations of Our Analysis

Our analysis is necessarily limited by the statistics and quality of the data set. We use data from the cruise phase of the Solar Orbiter mission (Zouganelis et al. 2020). Our period of data collection coincides with relatively quiet solar wind conditions, and the data set contains mostly slow solar wind observations. Instrumental effects on our observations have

been carefully evaluated in consultation with the SWA and MAG teams. Our rigorous application of the available quality filters to the data and our exchanges with the instrument teams have increased the reliability of our analysis. Our result in Figure 2 depends on the details of the method used to define the instability thresholds (see also Isenberg et al. 2013). Our method is, however, consistent with previous studies concerning the specific instabilities we consider (Hellinger et al. 2006; Bale et al. 2009). Our Figure 6 differs from the more straightforward $T_\perp$ dependence presented by D'Amicis et al. (2019), who find a positive correlation between θ_{BV} and $T_\perp$ in Alfvénic fast solar wind. However, this result does not contradict our analysis, given that we mostly observe slow solar wind in our data set.

5. Conclusions

We perform a statistical analysis of a large Solar Orbiter data set ($\sim$10^6 data points) to investigate the conditions necessary in the solar wind for the oblique firehose and mirror-mode instabilities to reduce temperature anisotropies. Our motivation is to use the newly available high-resolution data from the Solar Orbiter mission to explore energy transfer processes at small scales.

In our $T_\perp/T_\parallel$–$\beta_\parallel$ plot, we find that, while the investigated instabilities largely limit the plasma anisotropy, a significant
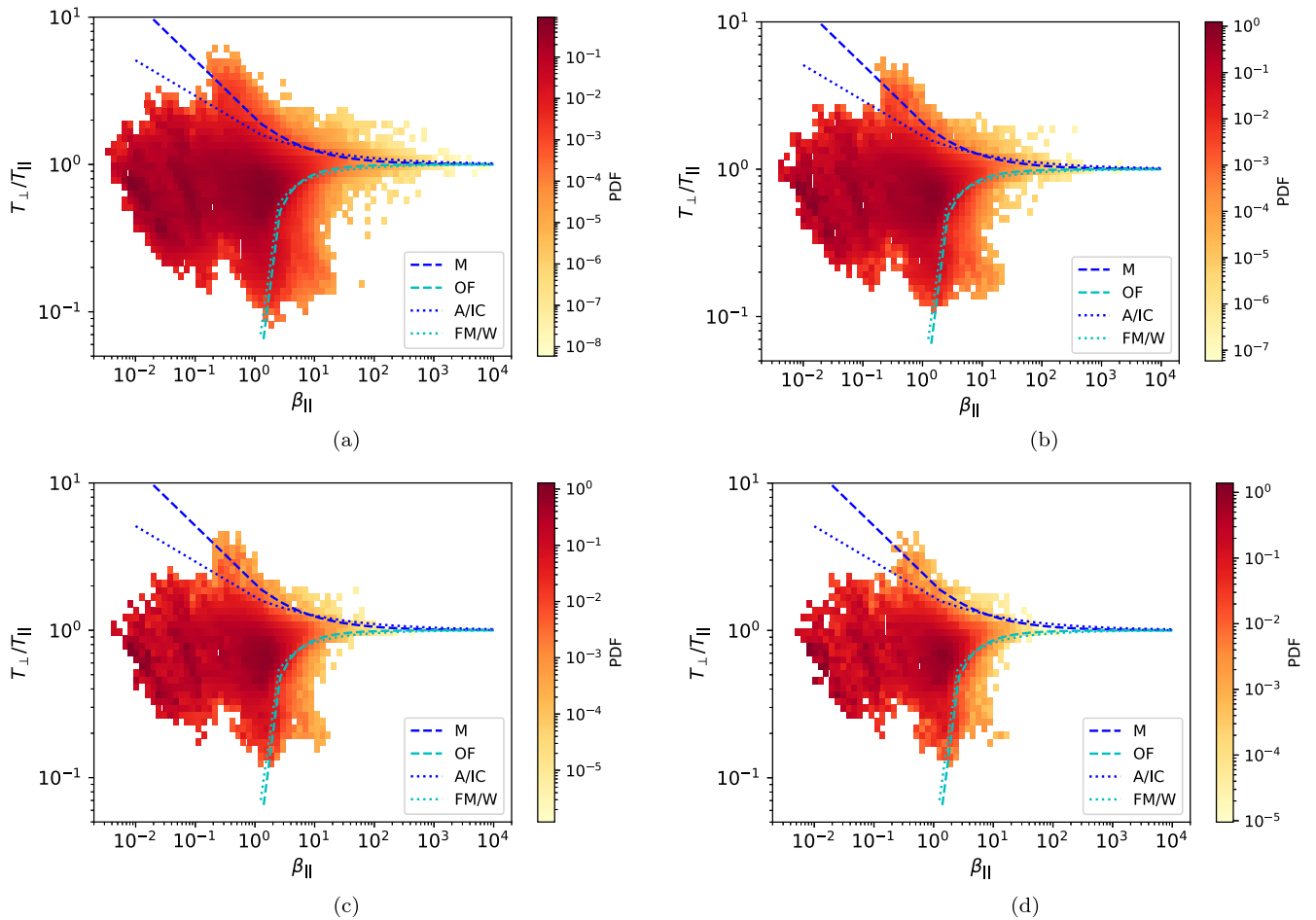
Figure 8. $T_\perp/T_\parallel$–$\beta_\parallel$ plots for averaged solar wind parameters with different averaging times. We overplot the instability thresholds according to Equation (1) for $\gamma_m = 10^{-2}\Omega_p$. The color-coding indicates the PDF of data points in each bin. The different panels represent averaging of data over subsequent sampling steps to simulate instruments with lower measurement cadences: (a) 4 s (original data set), (b) 12 s, (c) 48 s, and (d) 92 s.

number of data points ($\sim 3 \times 10^4$ for the oblique firehose and $\sim 4 \times 10^3$ for the mirror mode) lie in the unstable regions of parameter space. We interpret these as transient features whose full extent is revealed by the short measurement time (1 s) of the SWA instrument's PAS (Owen et al. 2020).

We explore the dependency of the distribution of oblique firehose and mirror-mode unstable solar wind intervals on θ_{BV} and find that the mirror-mode instability predominantly occurs when $\theta_{BV} \approx 0° \pm 45°$ or $\theta_{BV} \approx 180° \pm 45°$ and hence when $\mathbf{B}$ is close to the radial (or anti-radial) direction. By contrast, the peak in the PDF of the oblique firehose instability occurs when $\theta_{BV} \approx 75°$ or $\theta_{BV} \approx 255°$ and hence when $\mathbf{B}$ is close to a direction perpendicular to $\mathbf{V}$. This result suggests a predominant elevation of the temperature T_{TN} perpendicular to the radial direction relative to the temperature T_R in the radial direction for the unstable intervals, which is inconsistent with the predictions from the CGL double-adiabatic expansion of the solar wind alone. We interpret this dependency of the mirror-mode (oblique firehose) unstable plasma intervals on θ_{BV} as due to the presence (absence) of perpendicular ion heating from local, large-scale Alfvénic fluctuations.

In our analysis of θ_{BV}, we do not confine our considerations to Alfvénic wind intervals (D'Amicis et al. 2019; Louarn et al. 2021; Woodham et al. 2021) but instead concentrate on the relationship between θ_{BV} and the specific proton temperature anisotropy that drives the oblique firehose and mirror-mode

instabilities. This allows us to investigate the conditions needed for instabilities to act efficiently on the solar wind plasma and possible explanations for the occurrence of these conditions. However, our analysis is necessarily constrained by the statistical θ_{BV} distribution in our data set, which we expect to become less asymmetrical as more data are included while the Solar Orbiter mission continues.

We also measure the persistence of unstable solar wind intervals. The oblique firehose and mirror-mode instabilities require intervals of a size greater than about $34\rho_p$ and $24\rho_p$, respectively, in order to regulate the temperature anisotropy efficiently. These length scales are more clearly defined in units of ρ_p rather than in units of d_p. The minimum space to regulate anisotropy corresponds to approximately 2–3 typical wavelengths of the unstable mode at maximum growth rate.

Our work highlights the intricate connections between expansion effects, turbulence, and kinetic microinstabilities in the solar wind. Numerical simulations show that a combination of plasma expansion and strong 2D turbulence can drive both oblique firehose and mirror-mode instabilities (Hellinger et al. 2015, 2017). In addition, the spread of data in the $T_\perp/T_\parallel$–$\beta_\parallel$ parameter space is increased by pronounced small-scale intermittency in strong turbulence (Servidio et al. 2014). The combination of in situ instruments on the Solar Orbiter spacecraft allows us to study particle distributions with a very high time resolution, which helps to gain fresh insight into the

underlying processes (Adhikari et al. 2021; D'Amicis et al. 2021; Louarn et al. 2021; Nicolaou et al. 2021; Owen et al. 2021). We expect high-cadence in situ observations in combination with kinetic simulations of the expanding solar wind (Dong et al. 2014; Franci et al. 2015; Hellinger et al. 2015) to deliver further insights into this interplay in the future.

Appendix A
Averaging Effect

Our analysis in Figure 7 suggests that plasma instruments with low measurement cadence detect a lower proportion of unstable intervals than actually exist in the solar wind. In general, all instruments miss unstable intervals with a duration in the spacecraft frame comparable to the measurement cadence or shorter.

We simulate different measurement cadences by averaging our data over a successive number of sampling intervals. In Figure 8, we show the results averaged over 12, 48, and 92 s, compared with the base data set at 4 s cadence. The proportional share of data points in the regions of parameter space unstable to oblique firehose and mirror-mode instabilities increases with increasing cadence. At 4 s cadence, 3.12% of the data are oblique firehose unstable and 0.46% of the data are mirror-mode unstable. At 92 s, which corresponds approximately to the sampling cadence of the SWE instrument on board WIND, these numbers decrease to 2.45% for the oblique firehose instability and 0.31% for the mirror-mode instability. Moreover, the number of data points with extreme $\beta_\parallel$ values decreases significantly.

Appendix B
CGL Analysis

The double-adiabatic expansion according to the CGL theory is often considered an important contributor to the impact of expansion on the temperature anisotropy of the solar wind (Matteini et al. 2007; Verscharen et al. 2016). In this appendix, we evaluate the consistency of the CGL approach with our observations.

We start by assuming that the solar wind response to the expansion is consistent with the CGL equations (Chew et al. 1956):

$$\frac{d}{dt}\left(\frac{T_\perp}{B}\right) = 0 \tag{B1}$$

and

$$\frac{d}{dt}\left(\frac{T_\parallel B^2}{n_p^2}\right) = 0. \tag{B2}$$

When $\boldsymbol{B}$ is purely in the radial direction, $B \propto r^{-2}$ due to $\nabla \cdot B = 0$. Likewise, when $\boldsymbol{B}$ is purely in the tangential direction, $B \propto r^{-1}$ in a spherically symmetric configuration (Matteini et al. 2007, 2012; Hellinger et al. 2015). From Equations (B1) and (B2), we obtain

$$\frac{T_\perp}{T_\parallel} \propto \frac{B^3}{n_p^2}. \tag{B3}$$

Hence, under the assumption that $\boldsymbol{B}$ is purely radial, we find

$$\frac{T_\perp}{T_\parallel} \propto r^{-2}. \tag{B4}$$

Under the assumption that $\boldsymbol{B}$ is purely tangential, we find

$$\frac{T_\perp}{T_\parallel} \propto r. \tag{B5}$$

According to Equations (B4) and (B5), CGL double-adiabatic expansion in a smooth magnetic field predicts that $T_\perp/T_\parallel$ drops more quickly with r when $\boldsymbol{B}$ is in the radial direction than when $\boldsymbol{B}$ is in the tangential direction.

Assuming that the solar wind magnetic field obeys Parker's model, in which the Parker angle is a monotonously increasing function of r (Parker 1965), we expect conditions favorable for the oblique firehose instability especially when the field is quasi-radial. However, Figure 3 reveals the opposite behavior and even a higher occurrence of mirror-mode unstable intervals in the quasi-radial field geometry. This finding suggests that CGL double-adiabatic expansion alone does not provide a consistent explanation for the angular dependency result shown in Figure 3. The observed distribution of these instabilities contradicts the CGL prediction, suggesting that other processes must dominate the observed occurrence rates of unstable intervals.

ORCID iDs

Simon Opie ● https://orcid.org/0000-0002-2280-8807
Daniel Verscharen ● https://orcid.org/0000-0002-0497-1096
Christopher H. K. Chen ● https://orcid.org/0000-0003-4529-3620
Christopher J. Owen ● https://orcid.org/0000-0002-5982-4667
Philip A. Isenberg ● https://orcid.org/0000-0003-0505-8546

References

Adhikari, L., Zank, G. P., Zhao, L.-L., et al. 2021, A&A, 656, A6
Alexandrova, O., Chen, C. H. K., Sorriso-Valvo, L., Horbury, T. S., & Bale, S. D. 2013, SSRv, 178, 101
Bale, S. D., Kasper, J. C., Howes, G. G., et al. 2009, PhRvL, 103, 211101
Bruno, R., Bavassano, B., D'amicis, R., et al. 2006, SSRv, 122, 321
Bruno, R., & Carbone, V. 2013, LRSP, 10, 2
Bruno, R., Carbone, V., Primavera, L., et al. 2004, AnGeo, 22, 3751
Chandran, B. D. G., Dennis, T. J., Quataert, E., & Bale, S. D. 2011, ApJ, 743, 197
Chandrasekhar, S., Kaufman, A., & Watson, K. 1958, RSPSA, 245, 435
Chen, C. H. K. 2016, JPlPh, 82, 535820602
Chen, C. H. K., Matteini, L., Schekochihin, A. A., et al. 2016, ApJL, 825, L26
Chew, G., Low, F., & Goldberger, M. 1956, RSPSA, 236, 112
Cranmer, S. R., Asgari-Targhi, M., Miralles, M. P., et al. 2015, RSPTA, 373, 20140148
D'Amicis, R., Bruno, R., Panasenco, O., et al. 2021, A&A, 656, A21
D'Amicis, R., De Marco, R., Bruno, R., & Perrone, D. 2019, A&A, 632, A92
Dong, Y., Verdini, A., & Grappin, R. 2014, ApJ, 793, 118
Fox, N. J., Velli, M. C., Bale, S. D., et al. 2016, SSRv, 204, 7
Franci, L., Verdini, A., Matteini, L., Landi, S., & Hellinger, P. 2015, ApJL, 804, L39
Gary, S. P. 1993, Theory of Space Plasma Microinstabilities, Cambridge Atmospheric and Space Science Series (Cambridge: Cambridge Univ. Press)
Gary, S. P. 2015, RSPTA, 373, 20140149
Gary, S. P., Skoug, R. M., Steinberg, J. T., & Smith, C. W. 2001, GeoRL, 28, 2759
Hasegawa, A. 1969, PhFl, 12, 2642
Hellinger, P., Landi, S., Matteini, L., Verdini, A., & Franci, L. 2017, ApJ, 838, 158
Hellinger, P., Matteini, L., Landi, S., et al. 2015, ApJL, 811, L32
Hellinger, P., Trávníček, P., Kasper, J. C., & Lazarus, A. J. 2006, GeoRL, 33, L09101
Hellinger, P., & Trávníček, P. M. 2008, JGRA, 113, A10109
Hellinger, P., Trávníček, P. M., Štverák, U., Matteini, L., & Velli, M. 2013, JGRA, 118, 1351
Horbury, T. S., O'Brien, H., Carrasco Blazquez, I., et al. 2020, A&A, 642, A9
Howes, G. G. 2015, RSPTA, 373, 20140145
Howes, G. G., Cowley, S. C., Dorland, W., et al. 2006, ApJ, 651, 590
Howes, G. G., Cowley, S. C., Dorland, W., et al. 2008, JGRA, 113, A05103
Howes, G. G., TenBarge, J. M., Dorland, W., et al. 2011, PhRvL, 107, 035004
Isenberg, P. A., Maruca, B. A., & Kasper, J. C. 2013, ApJ, 773, 164
Kasper, J. C., Lazarus, A. J., & Gary, S. P. 2002, GeoRL, 29, 20
Kivelson, M. G., & Southwood, D. J. 1996, JGR, 101, 17365
Kiyani, K. H., Osman, K. T., & Chapman, S. C. 2015, RSPTA, 373, 20140155
Klein, K. G., Alterman, B. L., Stevens, M. L., Vech, D., & Kasper, J. C. 2018, PhRvL, 120, 205102
Klein, K. G., Kasper, J. C., Korreck, K. E., & Stevens, M. L. 2017, JGRA, 122, 9815
Kunz, M. W., Schekochihin, A. A., Chen, C. H. K., Abel, I. G., & Cowley, S. C. 2015, JPlPh, 81, 325810501
Kunz, M. W., Schekochihin, A. A., & Stone, J. M. 2014, PhRvL, 112, 205003
Kunz, M. W., Stone, J. M., & Quataert, E. 2016, PhRvL, 117, 235101
Louarn, P., Fedorov, A., Prech, L., et al. 2021, A&A, 656, A36
Lopez, R. A., Micera, A., Lazar, M., et al. 2022, ApJ, 930, 158
Marsch, E., Ao, X.-Z., & Tu, C.-Y. 2004, JGR, 109, A04102
Maruca, B. A., & Kasper, J. C. 2013, AdSpR, 52, 723
Maruca, B. A., Kasper, J. C., & Gary, S. P. 2012, ApJ, 748, 137
Matteini, L., Hellinger, P., Landi, S., Travnicek, P. M., & Velli, M. 2012, SSRv, 172, 373
Matteini, L., Landi, S., Hellinger, P., et al. 2007, GeoRL, 34, L20105
Matteini, L., Landi, S., Hellinger, P., & Velli, M. 2006, JGRA, 111, A10101
Matthaeus, W. H., Dasso, S., Weygand, J. M., et al. 2005, PhRvL, 95, 231101
Matthaeus, W. H., & Goldstein, M. L. 1982, JGR, 87, 6011
Matthaeus, W. H., Oughton, S., Osman, K. T., et al. 2014, ApJ, 790, 155
Müller, D., St. Cyr, O. C., Zouganelis, I., et al. 2020, A&A, 642, A1
Nicolaou, G., Verscharen, D., Wicks, R. T., & Owen, C. J. 2019, ApJ, 886, 101
Nicolaou, G., Wicks, R. T., Owen, C. J., et al. 2021, A&A, 656, A10
Ogilvie, K. W., Chornay, D. J., Fritzenreiter, R. J., et al. 1995, SSRv, 71, 55
Owen, C. J., Bruno, R., Livi, S., et al. 2020, A&A, 642, A16
Owen, C. J., Foster, A. C., Bruno, R., et al. 2021, A&A, 656, L8
Parker, E. N. 1965, SSRv, 4, 666
Parker, E. N. 1958, PhRv, 109, 1874
Pokhotelov, O. A. 2004, JGR, 109, A09213
Qudsi, R. A., Maruca, B. A., Matthaeus, W. H., et al. 2020, ApJS, 246, 46
Russell, C. T., Huddleston, D. E., Strangeway, R. J., et al. 1999, JGRA, 104, 17471
Schekochihin, A. A., Cowley, S. C., Dorland, W., et al. 2009, ApJS, 182, 310
Servidio, S., Osman, K. T., Valentini, F., et al. 2014, ApJL, 781, L27
Taylor, G. I. 1938, RSPSA, 164, 476
Treumann, R. A., Baumjohann, W., & Narita, Y. 2019, EP&S, 71, 41
Tu, C.-Y., & Marsch, E. 1995, SSRv, 73, 1
Verscharen, D., Chandran, B. D. G., Klein, K. G., & Quataert, E. 2016, ApJ, 831, 128
Verscharen, D., Chen, C. H. K., & Wicks, R. T. 2017, ApJ, 840, 106
Verscharen, D., Klein, K. G., & Maruca, B. A. 2019, LRSP, 16, 5
Verscharen, D., & Marsch, E. 2011, AnGeo, 29, 909
Wicks, R. T., Alexander, R. L., Stevens, M., et al. 2016, ApJ, 819, 6
Woodham, L. D., Horbury, T. S., Matteini, L., et al. 2021, A&A, 650, L1
Yoon, P. H. 2016, ApJ, 833, 106
Yoon, P. H., Sarfraz, M., Ali, Z., Salem, C. S., & Seough, J. 2021, MNRAS, 509, 4736
Zouganelis, I., De Groof, A., Walsh, A. P., et al. 2020, A&A, 642, A3